Noninvasive assessment of cutaneous wound healing using ultrahigh-resolution optical coherence tomography

Michael J. Cobb
Yuchuan Chen
University of Washington
Department of Bioengineering
Seattle, Washington 98195

Robert A. Underwood
Marcia L. Usui
John Olerud
University of Washington
Department of Medicine
Division of Dermatology
Seattle, Washington 98195

Xingde Li
University of Washington
Department of Bioengineering
Seattle, Washington 98195

Abstract. Ultrahigh-resolution optical coherence tomography (OCT) was used for noninvasive *in vivo* evaluation of the wound healing process. Cutaneous wounds were induced by 2.5-mm diameter full-thickness punch biopsies on the dorsal surface of seven mice. OCT imaging was performed to assess the structural characteristics associated with the healing process. The OCT results were compared to corresponding histology. Two automated quantitative analysis routines were implemented to identify the dermal-epidermal junction and segment the OCT images. Hallmarks of cutaneous wound healing such as wound size, epidermal migration, dermal-epidermal junction formation, and differences in wound composition were readily identified on the OCT images. Blister formation was also observed. Preliminary findings suggest OCT is a viable tool to noninvasively monitor wound healing *in vivo*. [DOI: 10.1117/1.2388152]

Keywords: optical coherence tomography; wound healing; image segmentation and imaging.

Paper 06093R received Apr. 7, 2006; revised manuscript received Jul. 7, 2006; accepted for publication Jul. 11, 2006; published online Nov. 10, 2006.

1 Introduction

Cutaneous wounds (e.g., burns, chronic skin ulcers, and surgical wounds) are among the most common wounds in clinical medicine. Each year in the United States, over 2 million people seek medical attention for burns,[1] and more than 6.5 million people are diagnosed with chronic skin ulcers.[2] In addition to aesthetically undesirable scarring, cutaneous wounds can become infected and lead to unnecessary morbidity or even death.[2] Accurate and timely assessment is critical for determining a correct treatment plan, which will affect the overall outcome of healing.

Wound healing is a complex and dynamic process that follows an orderly sequence of events. The sequence can be roughly divided into three distinct, yet sequentially overlapping phases—inflammation, granulation tissue formation, and tissue remodeling.[2,3] Characteristic structural changes associated with each phase could provide a basis for wound healing assessment with imaging technologies. After the inflammatory response begins, pronounced changes indicating normal wound healing include timely wound reepithelialization (i.e., lateral migration of epidermal cells across the wound bed), reformation of the dermal-epidermal junction (DEJ), thickening of the newly formed epidermis, and dermal remodeling. Having the tools to accurately monitor these changes is pivotal in identifying whether the wound undergoes a normal healing response, thereby enabling a timely decision for correct treatment.

Address all correspondence to Xingde Li, W. H. Foege Building, Room N430M, Box 355061, Seattle, Washington 98195-5061; Tel: 206-616-4853; Fax: 206-685-3300; E-mail: xingde@u.washington.edu

In laboratory research, invasive approaches such as chamber-embedding and biopsy are used to collect wound fluids (tissues) for biochemical assay and histology.[4–7] Other invasive methods include measurements of the tensile strength and electrical impedance of the wound.[8,9] Due to invasiveness, these methods are not common in clinical practice. Furthermore, biopsy is disruptive and introduces a new wound, precluding continuous assessment of the healing process in the same wound.

In clinical practice, wound size, color, odor, drainage, and eschar have been used for gross evaluation of wound healing.[10,11] Most of those parameters are obtained by direct surface measurement and visual observation. Those methods, however, do not provide structural information below the wound surface and can be very subjective, bearing considerable interobserver variability, which heavily depends upon the observer's experience, wound condition, and treatment history.[12]

To overcome the limitations of direct visual observations and to provide an objective assessment of the wound healing process, several noninvasive methods have been investigated including high-resolution ultrasound (HRUS),[13–16] confocal microscopy,[17–19] thermography,[20–23] transcutaneous pO_2,[24–27] laser Doppler imaging,[28] polarization imaging,[29,30] fluorescence imaging,[31] and magnetic resonance imaging (MRI).[32,33] Fluorescence imaging was used to look at the epidermal migration across the wound bed, MRI assisted with a contrast agent [albumin-(Gd-diethylenetriamine pentaacetic acid)] offered information about new vessel formation, and thermog-

1083-3668/2006/11(6)/064002/11/$22.00 © 2006 SPIE

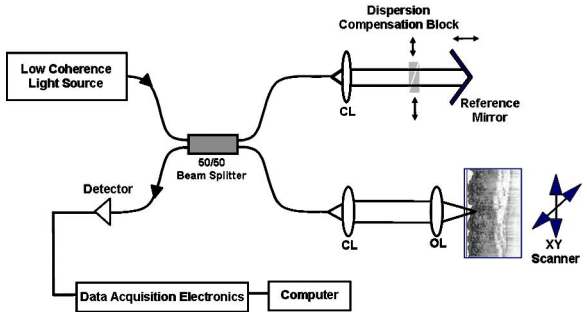

Fig. 1 Schematic of the fiber-optic OCT system used for the noninvasive assessment of the cutaneous wound healing process in a mouse model. The laser had an 825-nm center wavelength and a bandwidth of 155 nm, providing a measured axial resolution of ~2.8 μm in air. CL—collimating lens, OL—objective lens.

raphy provided indirect information about the wound healing process through temperature changes within the wound bed. HRUS was able to longitudinally monitor wound size and the formation of the DEJ and granulation tissue; however, the depth resolution (~75 μm) was insufficient to capture fine structural changes, such as wound reepithelialization or differentiation within the epidermis.[16] Additionally, ultrasound requires matching media in direct contact with the wound surface or dressing, which could irritate the wound and cause mechanical disruption of fragile wounded tissues.

Optical coherence tomography (OCT) is a noninvasive, fiber-optically based imaging technology, capable of real-time, cross-sectional imaging of biological tissues *in vivo* with a micrometer scale resolution.[34,35] OCT has a penetration depth of 0.5 to 3 mm in most highly scattering tissues, making it ideal for skin imaging and for assessing cutaneous wound healing. Recently, OCT combined with mulitphoton microscopy showed promising results in serial imaging of laser induced thermal injury and the subsequent healing effects in *in vitro* tissue constructs.[36] In addition, it has been shown that polarization sensitive OCT can quantitatively evaluate collagen denaturation induced by thermal injury and provide a correlation between burn depth and tissue birefringence.[1,37–40]

The objective of this study is to investigate the use of OCT to noninvasively monitor and identify the various stages in the wound healing process in a mouse model *in vivo*. Structural hallmarks of the healing process identified for assessment with OCT, include wound reepithelialization, formation of granulation tissue and the DEJ, epidermal thickening, and collagen remodeling.

2 Experimental Methods

2.1 *OCT*

The schematic diagram of the OCT system used in this study is shown in Fig. 1. Briefly, a 7- to 8-fs Ti:sapphire laser with a central wavelength of 825 nm and a full width at half maximum (FWHM) bandwidth of 155 nm was divided equally between a sample and a reference arm. The reference arm consisted of an adjustable dispersion compensation block and a retroreflector. The path length of the reference arm was varied by scanning a retroreflector at ~103 mm/s, generating a 250-kHz carrier frequency with a ~47-kHz bandwidth for the OCT interference signal. The sample arm had a microscope-type miniature beam delivery probe that focused the beam on the sample. The backscattered light from the sample arm was recombined with the reference at the 50/50 fiber-optic beamsplitter (combiner) and then sent to the detector. The interference fringes were amplified, filtered, logarithmically demodulated, and digitized for storage and display on a computer. Lateral beam scanning on the sample was achieved by a precisely controlled *x-y* scanner. The OCT system had a measured detection sensitivity of 103 dB with 3-mW incident power in the sample arm. For *in vivo* imaging, the power delivered to the cutaneous tissue was approximately 3 mW. The OCT axial resolution, as measured from the FWHM of the envelope of the cross-correlation fringe signal was ~2.8 μm (in air). The transverse resolution (Δx) was determined from the confocal parameter (b) according to $\Delta x = \sqrt{2b\lambda_0/\pi}$, where λ_0 is the center wavelength of the light source. The measured confocal parameter for our system was ~60 μm, which leads to a transverse resolution of ~5.6 μm.

2.2 *Animal Model and Cutaneous Wound Induction*

Seven heterozygous 8-to-10-week-old nondiabetic male mice (db^+/db^-) (BKS.Cg-m Lepr db/+, The Jackson Laboratory, Bar Harbor, Maine) were used to investigate the feasibility of OCT for noninvasive evaluation of cutaneous wound healing. The mice were housed in separate domiciles, with ad libitum access to food and water and kept on a 12-h light-dark cycle. All experimental procedures were performed in accordance with the protocols approved by the Institutional Animal Care and Use Committee at the University of Washington.

Hair removal, wound induction, position registration tattooing, and OCT imaging procedures were performed with the mice anesthetized using an intraperitoneal (IP) injection of a mixture of ketamine (100 mg/ml) and xylazine (20 mg/ml) 0.02 ml/g body weight. The dorsal skin was shaved and further treated with Nair (Church and Dwight Co., Inc, Princeton, New Jersey) to remove the hair. The shaved and Nair-treated skin was then cleansed with Betadine. Four full-thickness 2.5-mm diameter punch biopsy wounds were subsequently induced on the dorsal side of the mice. The wounds were covered with a semiocclusive dressing (Tegaderm) to help prevent scabbing, infection, and scratching.

2.3 *OCT Imaging Protocol*

Twenty-four hours after wound induction, two of the four unperturbed wounds were chosen for imaging with preference given to wounds closer to the tail since the corresponding motion artifact was less. The other two wounds were prepared in case either of the two chosen wounds became infected. One wound was imaged from head to tail, and the other wound was imaged from side to side (Fig. 2). Precise registration between a series of imaging time points was achieved by tattooing three small ink dots onto the skin adjacent to the wound with India ink, with two of the ink dots indicating imaging direction and the third ink dot indicating the orientation of the multiple imaging cross sections with respect to the straight line passing through the first two dots (Fig. 2). The registration was also used for correlating the OCT images with histology. The mouse was placed on its back in direct

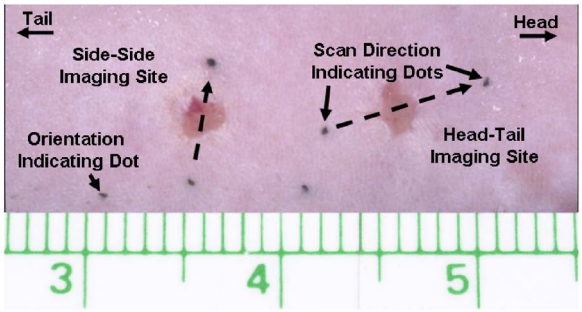

Fig. 2 Photograph of the induced full-thickness wounds on the dorsal side of the mouse. The image was aligned with the two ink dots across the wound. The third ink dot signified the orientation of the sequential scan direction (image between the two ink dots, move toward the third ink dot by a preselected distance, and then image across the wound again).

contact with a transparent 150-μm-thick cover glass window to minimize breathing-induced motion artifact. The imaging beam was aligned to the two ink dots, and two-dimensional registration was recorded and achieved using the *x*-*y* scanner. OCT imaging took place on each wound at three parallel locations at distances of 0, 100, and 500 μm, respectively, with respect to the line connecting the two ink dots. Each OCT image had a transverse size of 1 mm and multiple sequential cross-sectional images were taken between the two ink dots. After imaging between the ink dots, the *x*-*y* scanner moved the imaging beam 100 μm perpendicular to the line connecting the two ink dots in the direction indicated by third dot, and the imaging process along the new cross-section parallel to the first one was repeated. Once imaging at all three locations was finished, the beam was moved to the second wound site and the same procedure repeated. The wounds were imaged at days 1, 2, 3, 4, 6, 7, 10, and 12, following the time line shown in Table 1. Between imaging time points, the wounds were covered with a new piece of semiocclusive skin dressing (Tegaderm). One mouse was euthanized after imaging on day 3 and two mice were euthanized after imaging on each of days 4, 7, and 12 by an IP injection of a lethal dose of Euthasol. Imaged sites were immediately excised and fixed in 10% neutral buffered formalin.

Table 1 Imaging (X) and termination (X^T) time points for the seven mice used in the study.

	Day								
Mouse Number	1	2	3	4	5	6	7	10	12
1	X		X^T						
2	X	X		X		X	X	X	X^T
3	X		X		X	X	X^T		
4	X		X	X^T					
5	X			X^T					
6	X			X			X^T		
7	X			X			X	X	X^T

2.4 *Histological Processing and Registration*

Forty-eight hours after fixation, the excised tissue samples were prepared for histological processing by cutting one side parallel to the ink dots to ensure the histological section would be aligned with the OCT imaging cross sections. The samples were processed for routine paraffin embedding. Sections 5-μm thick were cut at the marked imaging sites perpendicular to the tissue surface and stained with hematoxylin and eosin (H&E). The OCT images were initially correlated with the histology micrographs using the two registration ink dots. Fine correlation was accomplished using morphological markers (e.g., hair follicles, wound region). The images were then evaluated by two independent observers to verify the correlation. OCT images and histology slides were concluded to correlate when both individuals were in agreement.

2.5 *OCT Image Analysis*

Time-dependent structural changes in the cutaneous wound healing process were assessed on all OCT images. The hallmarks used for identification included wound reepithelialization, formation of granulation tissue and the DEJ, epidermal thickening, and subsequent dermal remodeling. To facilitate the assessment process, automated DEJ estimation and segmentation routines were developed. The DEJ estimation routine approximated the location of the DEJ, while the segmentation routine provided information about structures within the epidermis and dermis. Epidermal thickness was measured from the estimated DEJ to the epidermal surface as determined from the automated segmentation routine.

2.6 *DEJ Estimation Routine*

There are many potential approaches to estimating the location of the DEJ.[41,42] As reported in Ref. 41, one approach is to first locate the tissue surface by finding the maximum value for each axial scan and then fit all the maximum values that fall within one standard deviation of the mean to a sixth-order polynomial. The DEJ is estimated to be the first local minimum between the tissue surface and the first local maximum after the surface. This method assumes the maximum intensity value for each axial scan is at the tissue surface, which may not always be the case, in particular when index matching fluid is used or when the focus is set deep within the tissue.

Here we focus on the trend of the OCT intensity changes within the tissue (i.e., below the tissue surface) along with an automatic routine based primarily on the Pan-Tompkins QRS detection method. In unwounded mouse skin, the OCT axial scan intensity revealed the following general trend: a decrease within the epidermis [see Fig. 3(b)], a transient increase (e.g., a transition) between the epidermis and dermis (DEJ), and then a decrease again within the dermis. Structures within the epidermis (i.e., granular, spinous, and basal cell layers) and dermis (e.g., collagen bundles, hair follicles) would scatter light differently and may cause additional slope changes in the axial scan [e.g., see the dermis region in Fig. 3(b)]. The DEJ

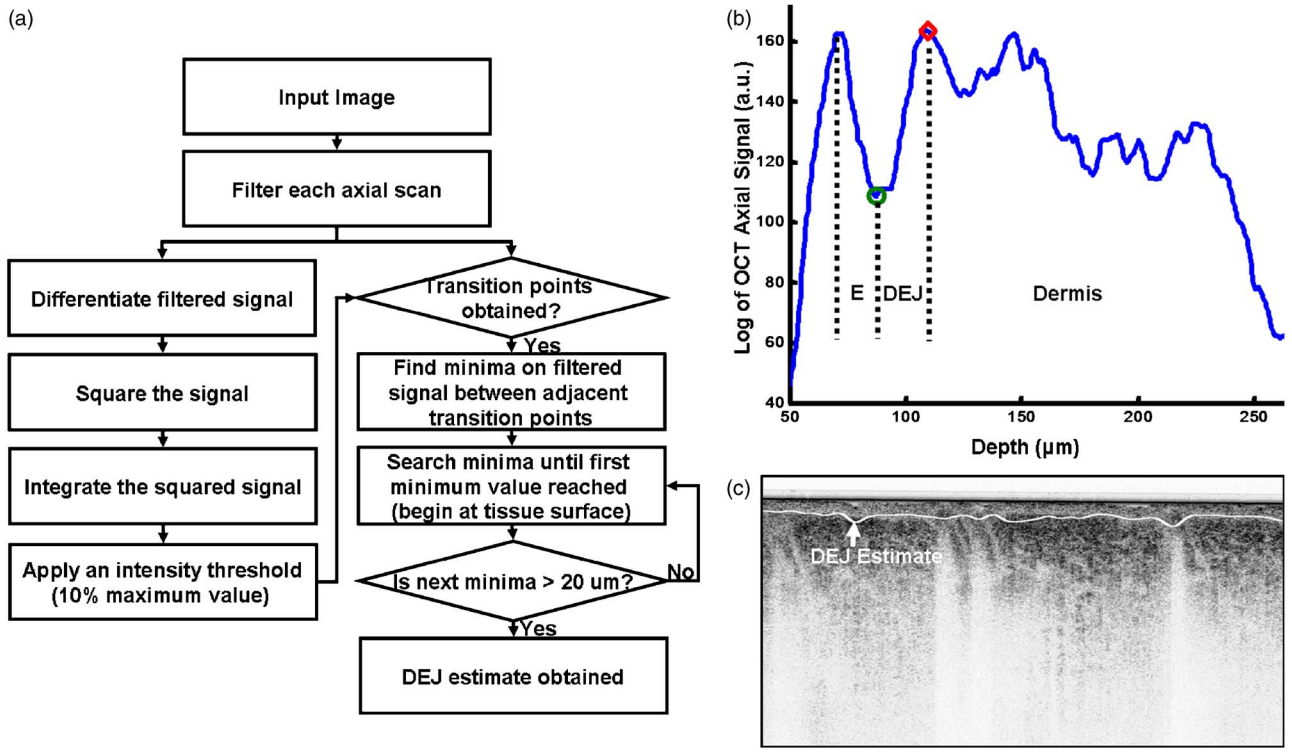

Fig. 3 DEJ estimation routine: (a) Flow chart of DEJ estimation routine. (b) Axial scan from unwounded mouse skin, showing the epidermal and dermal structures. The axial scan was low-pass filtered with a 50-tap moving-window filter. The region between the circular and diamond marks indicates the junction between the dermis and epidermis. The routine returns the beginning the DEJ estimate. (c) Image with the DEJ identified by the estimation routine. E—epidermis.

estimation algorithm aimed to find the first transition zone where the OCT intensity slope changes from negative to positive then to negative again.

The automatic estimation of the DEJ location was based on the fact the signal intensity undergoes strong transition over the junction between the epidermis and dermis [see Fig. 3(b)]. The procedure used a modified version of the Pan-Tompkins QRS detection algorithm [as outlined in Fig. 3(a)]. The Pan-Tompkins QRS algorithm is a standard heart rate detection algorithm,[43] which produces a pulse width that is proportional to the QRS width and the precise location of *R* waves. The algorithm also uses low amplitude thresholds to increase detection sensitivity. The basic procedure includes filtering the electrocardiographic signal, squaring the first derivate of the filtered data and then applying a moving window integrator to determine the position of the QRS complex. For this study, the tissue surface [i.e., the first peak on Fig. 3(b)] was chosen as the zero reference position for each axial scan. Each axial scan was low-pass filtered with a 50-tap smoothing filter (corresponding to a 20-μm-long axial segment) to reduce speckle noise and then differentiated to accentuate the transitions between structures, such as from epidermis to dermis. The differentiated signal was squared to amplify the sharper transitions and make the data positive. A moving window integrator, with a window size of 16 adjacent data points, was then passed over the squared data to further smooth the data.

In order to detect the stronger transitions or slope changes in the axial scan, and make the procedure less sensitive to noise, the transition points were defined as the locations where the integrated signal reached $\sim$10% of the overall maximum value of the integrated signal. The DEJ refers to the transition between the trough [i.e., the end of the epidermis as indicated by the green circle in Fig. 3(b)] and the following maximum (i.e., the beginning of the dermis as indicated by the red diamond). In the DEJ estimation routine, we used the transition points detected by the modified Pan-Tompkins algorithm to locate the first trough (minimum) as the consistent estimate of the beginning position of the DEJ. The DEJ estimation routine was applied to the OCT time series, and the results are shown in Fig. 6 (see white line).

2.7 *Image Segmentation*

In order to objectively determine structures within the OCT image, a simple segmentation routine was applied to each OCT image. The segmentation routine [as outlined in Fig. 4(a)] consisted of five steps: (1) median filtering, (2) threshold via hysteresis, (3) image dilation, (4) filling in isolated pixels, and (5) performing Canny's edge detection.[44]

The first step in the segmentation routine applied a 5×5 median filter four times to the original OCT image to reduce speckle noise. The 5×5 kernel was chosen to roughly match the OCT axial resolution of 2.0 μm in tissue (e.g., five pixels correspond to roughly 2.0 μm).

After filtering, a hysteresis threshold method was used to create a binary image. Hysteresis threshold is a commonly used two-stage threshold technique in edge detection and segmentation routines,[44–47] and works by applying an upper and

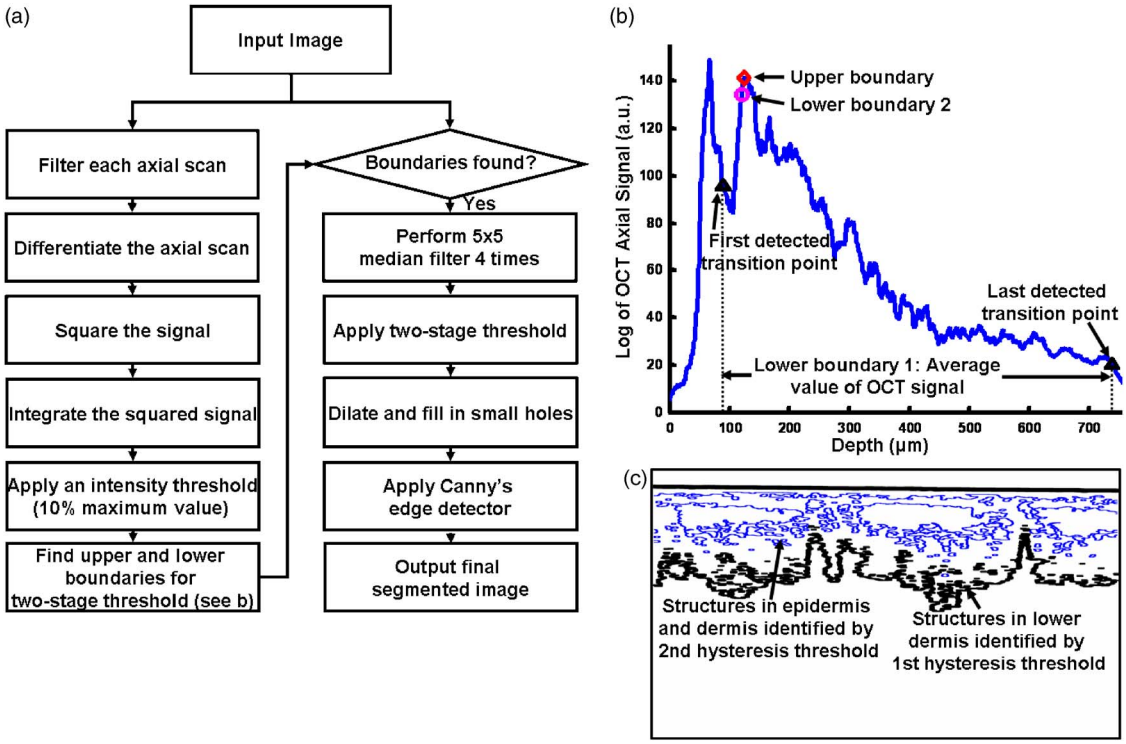

Fig. 4 OCT image segmentation routine: (a) Flow chart of OCT image segmentation routine. (b) Low-pass filtered axial scan from unwounded mouse skin, showing the automatically detected hysteresis threshold values. For each axial scan, the first hysteresis threshold had an upper boundary indicated by the red diamond and the filtered axial scan was averaged between the two black triangles to determine the lower boundary. The second hysteresis threshold used the same upper boundary (indicated by he red diamond), while the lower boundary was set to 95% of the upper threshold (magenta circle). The average upper and lower boundary over all axial scans in an image was used for the hysteresis threshold to produce the segmented image in (c). (c) Resultant edge detected image. The first hysteresis threshold produced the thick black line and represents the lower portion of the dermis. The second hysteresis threshold produced the blue region (thin line) and illustrates structures within the dermis and epidermis (color online only).

lower intensity threshold to the image. The upper threshold defines the initial object boundary, and all pixels greater than the threshold are immediately set to 1 on the final binary image. The lower threshold identifies the background level of the image and simply sets all pixels greater than the threshold to 1 and those less to 0. The location of each pixel (with a value 1) identified by the lower threshold is then compared to those identified by the upper threshold. If the pixel identified by the lower threshold is adjacent to a pixel with a value of 1 identified by the upper threshold, the pixel is defined as part of the object and set to 1 on the final binary image; otherwise, it is set to 0.

The binary image is then dilated using a 5×5 mask, and any remaining "holes" after dilation are set to 1. A hole is any pixel with a value of 0 that cannot be reached from the edge of the image (e.g., a 0 pixel in the middle of an object). Canny's edge detector[44] is then applied to the resultant image to obtain the object boundaries. Canny's edge detector works by smoothing the image with a Gaussian mask and then locating the gradient of the smoothed image to highlight regions with high special derivatives. Values not at the maxima in the gradient array are suppressed (i.e., nonmaxima suppression), and then a hysteresis threshold is applied to the data to produce the object's boundaries.

In our study, two different hysteresis thresholds were used to generate two segmented images. The two segmented images were added together to form the final segmented image [shown in Fig. 4(c)]. The upper and lower boundaries for both hysteresis thresholds were determined automatically from the transition points detected in the DEJ estimation algorithm. Both hysteresis thresholds used the same upper boundary. The upper boundary was chosen to primarily detect structures within the dermis and neglected the influence of back reflection from the tissue surface. Considering the tissue surface [i.e., the first peak on Fig. 4(b)] was set to the zero reference position in the DEJ estimation algorithm, the first detected transition point [i.e., the first black triangle in Fig. 4(b)], which was determined by following the same procedure as described in the above DEJ estimation routine would fall after the tissue surface. The upper boundary was set to the overall maximum intensity of the filtered A-scan [see Fig. 4(b), red diamond] after the first detected transition point or slope change. In general, for unwounded mouse skin, the upper boundary was the maximum point within the dermis. The lower boundary was set at the mean intensity on the filtered A-scan between the first and last detected transition points [see Fig. 4(b), black triangles], which should primarily contain signals from the dermal layer of the tissue. The second hysteresis threshold had the same upper boundary as the first hysteresis threshold and the lower boundary was set to 95% the upper boundary [see Fig. 4(b), magenta circle]. The 95% upper boundary was chosen arbitrarily to provide information

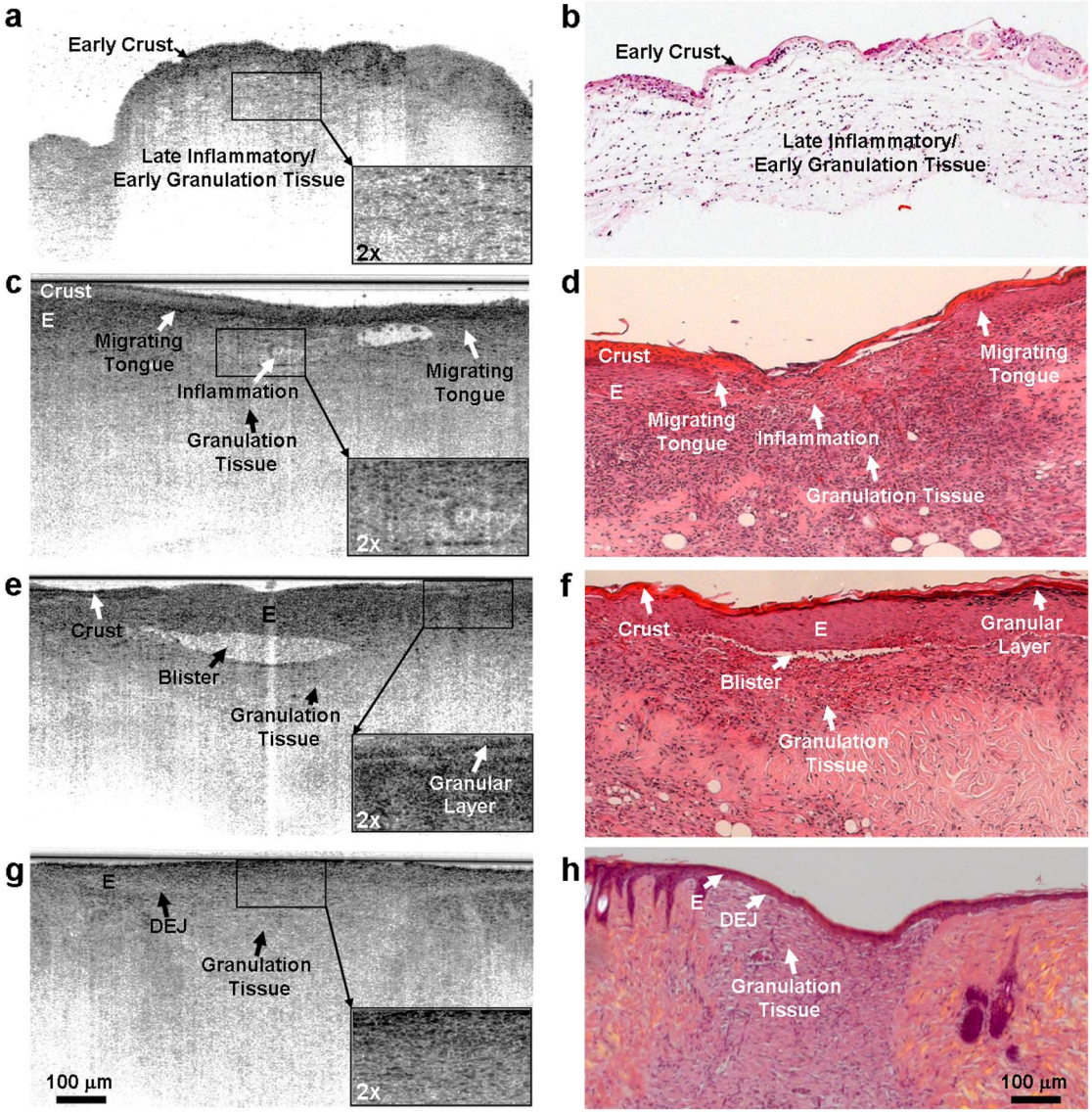

Fig. 5 OCT images [(a), (c), (e), (g)] and the corresponding histology [(b), (d), (f), (h)] taken at 3 [(a), (b)], 7 [(c) to (f)], and 12 [(g), (h)] days post wound induction. (a), (b) OCT image taken at 3 days post wound induction and (b) corresponding histology showing the transition from the inflammatory response to the formation of granulation tissue. The inset shows a 2× zoomed view of the late inflammatory (early granulation) tissue on the OCT image. The small covering on the surface is a crustlike formation to protect the wound bed. (c), (d) OCT (c) and corresponding histology (d) image taken at 7 days post wound induction, near the center of the wound bed. The epidermal layer (E) is migrating across the wound bed. Inflammatory cells are still present, but the wound bed is now mainly composed of granulation tissue. A magnified view of the inflammatory tissue is shown in the lower right-hand corner of the image. (e), (f) OCT (e) and corresponding histology (f) image taken at 7 days post wound induction, from the same mouse as (c), (d), but closer to the wound edge. The epidermal layer is thicker than an unwounded epidermis. Differentiation is beginning to take place in the epidermis, with the granular layer becoming visible (see inset in lower right-hand corner). Additionally a blister has developed between the newly formed epidermis and granulation tissue. (g), (h) OCT (g) and corresponding histology image (h) taken at 12 days post wound induction. The DEJ has formed across the wound bed. The granulation tissue has more extracellular matrix and collagen present. The OCT and histology image size is roughly 1×0.6 mm in tissue (transverse×depth). The incident power on the mouse skin was ~3 mW.

on the strongly backscattering tissue components (e.g., collagen). The process for determining the upper and lower boundaries was repeated for each axial scan in the image, and the average value obtained was used to threshold the image. We found that the first hysteresis threshold primarily identified structures in the lower portion of the dermis [see Fig. 4(c), thick black line], while the second hysteresis threshold primarily determined structures in the epidermis and dermis [shown in Fig. 4(c), thin blue line]. The segmentation routine was applied to the OCT time series, shown in Fig. 6

3 Results

High-resolution OCT time-series images of full-thickness cutaneous wounds were obtained during the course of wound healing. All the mice survived anesthesia, wound induction,

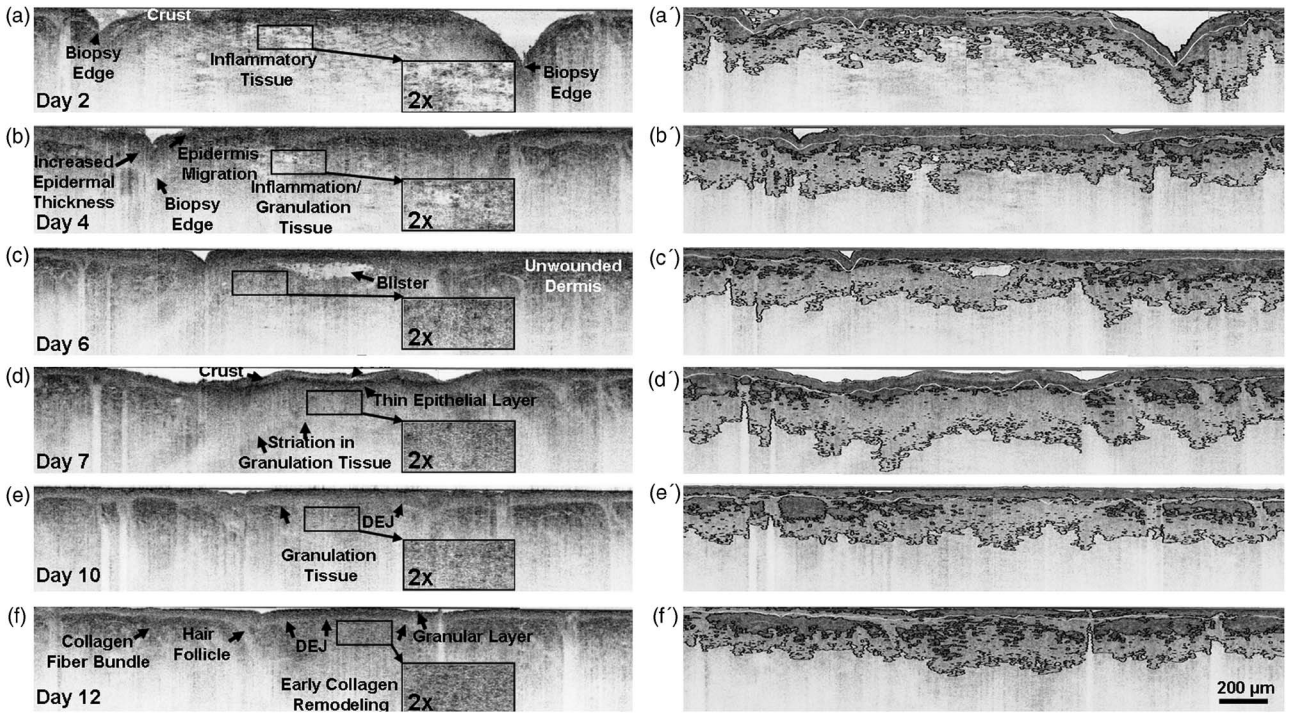

Fig. 6 OCT longitudinal time sequence for one mouse over 12 days. The changes in the wound bed over the 12-day time course is shown in the 2×-zoomed inset for each day. The sequence shown on the right [(a′) to (f′)] is the output from the DEJ and image segmentation routines. (a), (a′) Day 2: The wound bed is filled with loosely packed extracellular matrix comprised of early granulation tissue and inflammatory cells. (b), (b′) Day 4: The epidermis immediately adjacent to the wound has grown thicker and has begun to migrate laterally across the wound bed. The loosely packed extracellular matrix is becoming denser. (c), (c′) Day 6: A thin epithelium now stretches across the wound bed. A blister has formed between the epithelial layer and granulation tissue. The granulation tissue has begun to differentiate. (d), (d′) Day 7: The epithelial layer and delineation within the granulation tissue are becoming more evident. (e), (e′) Day 10: The DEJ is beginning to form. (f), (f′) Day 12: The DEJ has completely formed across the wound bed. The epidermis is contracting and differentiation is taking place. The granulation matrix is becoming dominated by collagen. The incident power on the mouse was ~3 mW. The image size is ~2.45×0.45 mm in tissue (transverse×depth).

and the OCT imaging procedure without incident. Each OCT image took ~12 s to collect and the average total imaging time for one mouse was approximately 10 to 20 min. The OCT images were scaled by an average skin refractive index of ~1.4.[48]

3.1 *OCT—Histology Correlation*

Figure 5 shows four representative OCT images (1 ×0.6 mm, transverse×depth, in tissue) and the corresponding histology micrographs. The images were taken at 3 [Figs. 5(a) and 5(b)], 7 [Figs. 5(c)–5(f)], and 12 [Figs. 5(g) and 5(h)] days after wound induction.

As shown in Figs. 5(a) and 5(b) (three days after the wound induction), the late inflammatory/early granulation tissue nonuniformly backscatters light, giving the appearance of a loosely packed material. The small crust (or eschar) present on the wound surface to protect the wound bed appears slightly more scattering and uniform than the late inflammatory/early granulation tissue. The inflammatory tissue and crust are marked on the OCT image and correlate well with the corresponding histology [Fig. 5(b)].

Seven days after wound induction, the migrating tongue of the newly formed epidermis, late inflammatory tissue, crust, and granulation tissue can clearly be seen on the OCT image [Fig. 5(c)], which correlates with the corresponding histology [Fig. 5(d)]. The crust is more uniform in appearance than on day 3. The granulation tissue backscatters the light similar to, but has a denser appearance than, the loosely packed inflammatory/early granulation tissue OCT image [Fig. 5(a)].

Additional structures revealed in the OCT image [Fig. 5(e)] from day 7 are the upper granular layer of the epidermis and blister. The granular layer shows up as a highly backscattering thin line across the top of the epidermis. The epidermis seems more backscattering than the granulation tissue. A blister (i.e., fluid-filled low scattering pocket) lying between the epidermis and granulation tissue in the OCT image [Fig. 5(e)] was confirmed by corresponding histology [Fig. 5(f)].

Figures 5(g) and 5(h) show the healing stage 12 days after wound induction and reveals mature and newly formed epidermis, dermis, and DEJ. The granulation tissue appears more uniform and less grainy than in earlier days and is beginning to resemble the adjacent mature, collagen-rich dermis. The junction between the newly grown epidermal and dermal tissues has become more visible on the OCT image [Fig. 5(g)] than in previous days. All structures marked on the OCT image [Fig. 5(g)], are confirmed with the corresponding histology [Fig. 5(h)].

3.2 *OCT Time Series*

OCT imaging was longitudinally performed over a 12-day period (Fig. 6) to monitor the wound healing process in one mouse over the same wound area. The OCT images had a

Table 2 Changes in the wound size for one mouse over 12 days.

Day	Wound Size	Change from Previous Day
2	1.905 mm	N/A
4	1.425 mm	0.480
6	1.010 mm	0.415
7	1.010 mm	0
10	0.735 mm	0.275
12	0.635 mm	0.100

physical dimension of $\sim 2.45 \times 0.45$ mm in tissue. The automated DEJ estimate and segmentation routines were applied to the OCT images [shown in Figs. 6(a) to 6(f)], with the output shown in Figs. 6(a′) to 6(f′), and were used to aid in identifying the DEJ and structures within the mouse skin. The wound region could be distinguished over the entire time sequence, using the hair follicles, punch biopsy edges, dermal content (granulation versus collagen-rich tissue) and epidermal thickness as reference points. The wound size was measured near the top of the wound using the wound margins and hair follicles as boundaries. As indicated in Table 2, the wound size decreases during the healing process.

Two days after wound induction [Fig. 6(a)], a crustlike structure covers the wound bed and the bed itself appears disorganized. At the edge of the wound, the deep cuts caused by the punch biopsy are clearly visible. The boundary of the epidermis adjacent to the wound can be clearly seen. By day 4 [Fig. 6(b)], the epidermis immediately adjacent to the wound has grown thicker and begun to migrate laterally across the wound. The loosely packed tissue in the wound bed is becoming denser and more organized, similar to late inflammatory/early granulation tissue shown in Fig. 5(a). The OCT image of the wound bed at day 6 [Fig. 6(c)] has similar structures as the OCT image of the blister shown in Fig. 5(e). Granulation tissue has formed in the wound bed with a thin epithelial layer completely covering the wound bed. A blister was identified between the thin epithelium and the granulation tissue. On day 7 [Fig. 6(d)], the crust begins to tear away from the newly formed epithelial layer. The epithelial layer and delineation within the granulation tissue are more evident than in previous days. The epidermis adjacent to the wound starts to return to its original state. By day 10 [Fig. 6(e)], there is clearer distinction between the newly grown epidermal and dermal layers. The DEJ is visible near the edge of the wound and the granulation tissue is becoming more dense (e.g., darker on the OCT image) and more uniform. The regrown epidermal thickness, as determined by the distance from the tissue surface to the DEJ estimated from the automated segmentation routine, is $\sim 45 \pm 5.9$ μm. All epidermal thickness measurements were taken over at least eight images. The wound bed at day 12 [Fig. 6(f)] has more mature granulation tissue present and a clearly defined epidermis covering it. The DEJ has completely formed across the wound bed and the epidermis over the wound bed is becoming slightly thinner ($\sim 41 \pm 4.5$ μm versus $\sim 45 \pm 5.9$ μm at day 10).

4 Discussion

This study demonstrated that ultrahigh-resolution OCT is a promising tool for noninvasively monitoring cutaneous wound healing process *in vivo*. OCT images revealed the orderly cutaneous wound healing process. Differences in tissue structures over the 12-day wound healing process were clearly identified and correlated well with the corresponding histology and published expectations.[2,3,12,49–51]

One of the first noticeable changes in preparation for epidermal migration [day 4, Fig. 6(b)] is the thickening of the epidermis immediately adjacent to the wound probably due to the mitotic activity of nearby basal cells.[3,52] Wound reepithelialization then begins with the migration of epithelial cells laterally across the wound bed,[2,3,49] which can be seen at day 4. By day 6, the migrating epithelial cells completely cover the wound bed and form a thin epithelial layer (which is more clearly seen on day 7) [Figs. 6(c) and 6(d)] as expected.[3] Thickening of the epithelial layer takes place up to day 10 [Fig. 6(e)]. By day 12, the epidermis is ~ 41 μm [Fig. 6(f)], thinner than day 10, indicating that the process of epidermal contraction has begun. In addition to epidermal contraction, differentiation within the epidermis is evident with a thin reflective granular layer present near the surface [see Figs. 5(e) and 6(f)].

The composition of the wound bed changed dramatically over the 12-day time course, as expected. In general, when a wound heals, the wound bed composition will proceed from inflammatory tissue to granulation tissue. Eventually, collagen will dominate the granulation tissue.[2] During the initial days after wound induction, backscattering from the wound bed appears nonuniform on the OCT image [Fig. 6(a)], which most likely correlates with inflammatory tissues. On day 4 [Fig. 6(b)], the wound bed becomes denser and more uniformly backscattering, correlating to the late inflammatory/early granulation stage [Fig. 5(b)], during which macrophages, blood vessels, and fibroblasts infiltrate the wound bed and replace the inflammatory cells. The granulation tissue has completely formed in the wound bed by day 6 [Fig. 6(c)] and has fairly uniform optical backscattering. As time progresses, the granulation tissue becomes more strongly backscattering, owing to an increase in collagen, which has a higher refractive index of ~ 1.5 compared to ~ 1.36 for the remaining extracellular matrix.[53] The granulation tissue present at day 12 [Figs. 6(f) and 6(f′)] more strongly backscatters light than at previous days, suggesting an increase in the collagen content and early collagen remodeling is taking place. OCT was able to visualize not only the formation of granulation tissue, but also differences within the granulation tissue [see Figs. 6(d) and 6(d′)]. Overall, the structural hallmarks associated with the wound healing process identified for this study, such as wound reepithelialization and subsequent epidermal thickening, granulation tissue formation and so on, were consistently visualized in the OCT images from all seven mice.

In addition to monitoring wound composition, OCT was able to measure wound size at the different imaging time points. The 2.5-mm diameter wound will typically take ~ 13 days for wound closure to occur in normal mice.[12] The initial wound size identified by OCT is ~ 0.600 mm smaller than the size of the punch biopsy cylinder, which is most likely due to the immediate tissue contraction after punch biopsy.[12] The

wound size was measured using the wound margins identified on OCT images at days 2 and 4. For days 6 to 12, hair follicles were used as the wound boundaries, because hair follicles cannot grow in the newly formed wound bed. The results shown in Table 2 suggest OCT can conveniently monitor the wound size *in vivo*.

During the healing process, OCT was able to clearly and consistently identify blisters [see Figs. 5(c), 5(d), and 6(c)], which prior to this observation were thought to be artifacts of histology processing. Immediately following wound reepithelialization, the thin epithelial layer is only loosely connected to the granulation tissue. This loose connection can give rise to a blister due to internal or external mechanical stress, in which the epidermis separates from the granulation tissue. Blisters were visualized in 75% of the wounds imaged on days 6 and 7. As the epithelial layer becomes thicker and the DEJ forms, the formation of blisters diminishes. The DEJ begins to appear by day 10 and completely bridges the wound by day 12, which is consistent with reported cutaneous wound healing time course results for a 2.5-mm-diameter cutaneous wound in a normal mouse model.[12] The DEJ protects against mechanical trauma by anchoring the epidermis to the dermis. No blisters were observed on the OCT images at day 10 or day 12.

The DEJ estimation routine adapted for this study was able to consistently distinguish between the epidermal and dermal layers in the unwounded tissue. The DEJ estimate across the wound bed before day 10 is not reliable, because the DEJ has yet to form. The DEJ estimate on day 12 shows the DEJ has formed completely across the wound bed. The variation present in the estimate at day 7 is caused by the presence of the crust layer. The DEJ estimate used a simple thresholding approach to locate the transition between the epidermis and dermis and could possibly be improved by more sophisticated techniques.[42]

The OCT image segmentation routine employed was able to accurately discern differences in both wounded and unwounded tissue [see Figs. 6(a′) to 6(f′)]. In the unwounded tissue, interfollicular collagen and hair follicles can be clearly seen [see Fig. 6(f′)]. During the wound healing time course, the blister was segmented out at day 6 and striations in the wound bed can be seen at day 7. The difference in the wound bed between days 10 and 12 shows a possible increase in collagen content and a more stable DEJ estimate. The segmentation routine could be further improved by implementing a more adaptive routine to provide the hysteresis threshold values for specific regions of interest.

The light power delivered to the tissue (i.e., ~3 mW) is less than the maximum permissible exposure outlined by the American National Standards Institute.[54] In addition, OCT imaging was performed in a noncontact fashion; thus imaging caused no damage to the wound, allowing noninvasive monitoring of the healing process. The time to collect an image was ~12 s. Real-time, ultrahigh-resolution OCT imaging at 12 to 20 frames per second (1000×2000 pixels, transverse $\times$ depth) became available in our laboratory by using a spectrum domain technique.[55–59] In future studies, this will enable monitoring of the wound bed at or near video rate and dramatically reduce the time needed to scan over the entire wound. Consequently, rapid construction of larger volumetric data sets over the entire wound bed (i.e., 3D-OCT) will become feasible, providing a more comprehensive snapshot of the wound condition over the entire wound bed.

The findings presented here demonstrate that OCT is a viable tool for noninvasively monitoring the structural hallmarks of wound healing *in vivo*. OCT shows the formation and migration of the thin epithelial layer over the wound bed, as well as the subsequent thickening and contraction. We were able to observe epidermal, DEJ, and dermal wound healing benchmarks.

Further insight into the wound healing process can be enhanced by combining the structural OCT with functional OCT methods. For instance, Doppler OCT could be very attractive for assessing the formation of new blood vessels within the wound bed.[60,61] In addition, structural and/or functional OCT imaging could also be used to determine the effect of drug treatment on wound healing. OCT not only provides noninvasive assessment of wound healing, but reduces potential interobserver bias. The successful preliminary results shown here and elsewhere[36,40] suggest a promising role for OCT in noninvasive monitoring of wound healing *in vivo*.

Acknowledgments

The authors would like to thank Dr. Yansong Gu for his assistance with the histology correlations. This research was supported in part by the Whitaker Foundation, National Institutes of Health, the National Institute of Dental and Craniofacial Research Predoctoral Training Fellowship (M. J. C.), and the National Science Foundation CAREER Award (X. D. L.).

References

1. B. S. Atiyeh, S. W. Gunn, and S. N. Hayek, "State of the art in burn treatment," *World J. Surg.* **29**(2), 131–148 (2005).
2. A. J. Singer and R. A. F. Clark, "Mechanisms of disease—Cutaneous wound healing," *N. Engl. J. Med.* **341**(10), 738–746 (1999).
3. R. Cotran, V. Kumar, and T. Collins, *Robbins Pathologic Basis of Disease*, 6 ed., W. B. Saunders Company, Philadelphia (1999).
4. F. Gottrup, M. S. Agren, and T. Karlsmark, "Models for use in wound healing research: A survey focusing on *in vitro* and *in vivo* adult soft tissue," *Wound Repair Regen* **8**(2), 83–96 (2000).
5. T. K. Hunt, P. Twomey, B. Zederfeldt, and J. E. Dunphy, "Respiratory gas tensions and pH in healing wounds," *Am. J. Surg.* **114**(2), 302–307 (1967).
6. J. A. Schilling, W. Joel, and H. M. Shurley, "Wound healing: A comparative study of the histochemical changes in granulation tissue contained in stainless steel wire mesh and polyvinyl sponge cylinders," *Surgery (St. Louis)* **46**, 702–710 (1959).
7. G. D. Winter, "Formation of the scab and the rate of epithelization of superficial wounds in the skin of the young domestic pig," *Nature (London)* **193**, 293–294 (1962).
8. J. E. Olerud, G. F. Odland, E. M. Burgess, C. R. Wyss, L. D. Fisher, and F. A. Matsen, "A model for the study of wounds in normal elderly adults and patients with peripheral vascular-disease or diabetes-mellitus," *J. Surg. Res.* **59**(3), 349–360 (1995).
9. L. Adam, A. Tadmor, E. Aizinbud, and H. Schindler, "Electrical impedance monitoring of the wound-healing process," *Med. Prog. Technol.* **9**(4), 227–232 (1983).
10. A. B. Wysocki, "Wound measurement," *Int. J. Dermatol.* **35**(2), 82–91 (1996).
11. J. Z. Cuzzell, "The new RYB color code," *Am. J. Nurs.* **88**(10), 1342–1346 (1988).
12. S. R. Sullivan, R. A. Underwood, N. S. Gibran, R. O. Sigle, M. L. Usui, W. G. Carter, and J. E. Olerud, "Validation of a model for the study of multiple wounds in the diabetic mouse (db/db)," *Plast. Reconstr. Surg.* **113**(3), 953–960 (2004).

13. P. Mantis, D. H. Lloyd, D. Pfeiffer, K. Stevens, S. Auxilia, C. Noli, and F. Abramo, "High-resolution ultrasonography of experimentally induced full-thickness canine skin wounds: Efficacy in imaging canine skin and comparison of 2 methods of measuring wound size," *Wounds* **17**(5), 107–113 (2005).
14. R. J. Whiston, J. Melhuish, and K. G. Harding, "High-resolution ultrasound imaging in wound-healing," *Wounds* **5**(3), 116–121 (1993).
15. J. E. Olerud, W. O'Brien, Jr., M. A. Riederer-Henderson, D. Steiger, F. K. Forster, C. Daly, D. J. Ketterer, and G. F. Odland, "Ultrasonic assessment of skin and wounds with the scanning laser acoustic microscope," *J. Invest. Dermatol.* **88**(5), 615–623 (1987).
16. M. Dyson, S. Moodley, L. Verjee, W. Verling, J. Weinman, and P. Wilson, "Wound healing assessment using 20 MHz ultrasound and photography," *Skin Res. Technol.* **9**(2), 116–121 (2003).
17. H. D. Cavanagh, M. S. El-Agha, W. M. Petroll, and J. V. Jester, "Specular microscopy, confocal microscopy, and ultrasound biomicroscopy—Diagnostic tools of the past quarter century," *Cornea* **19**(5), 712–722 (2000).
18. S. J. Chew, R. W. Beuerman, and H. E. Kaufman, "Real-time confocal microscopy of keratocyte activity in wound-healing after cryoablation in rabbit corneas," *Scanning* **16**(5), 269–274 (1994).
19. N. J. Vardaxis, T. A. Brans, M. E. Boon, R. W. Kreis, and L. M. Marres, "Confocal laser scanning microscopy of porcine skin: Implications for human wound healing studies," *J. Anat.* **190**, 601–611 (1997).
20. T. W. Dickerson, R. C. Youngblood, P. L. Ryan, and S. T. Willard, "Use of digital infrared thermography to assess rate of wound healing in a murine model," *FASEB J.* **18**(5), A1184–A1185 (2004).
21. H. W. Pau, U. Sievert, and W. Wild, "Thermography of the skin covering a cochlear implant—Temperature as an indicator for blood circulation," *Laryngol., Rhinol., Otol.* **82**(9), 615–619 (2003).
22. E. M. Weilermithoff, "Infrared thermography and trans-cutaneous oxymetry in the assessment of wound-healing under local-administration of tetrachlordecaoxide (Oxiliumr)," *J. Photogr. Sci.* **37**(3–4), 185–188 (1989).
23. M. Horzic, D. Bunoza, and K. Maric, "Contact thermography in a study of primary healing of surgical wounds," *Ostomy Wound Manage* **42**(1), 36–38, 40–42, 44 (1996).
24. S. Park, O. M. Tepper, R. D. Galiano, J. M. Capla, S. Baharestani, M. E. Kleinman, C. R. Pelo, J. P. Levine, and G. C. Gurtner, "Selective recruitment of endothelial progenitor cells to ischemic tissues with increased neovascularization," *Plast. Reconstr. Surg.* **113**(1), 284–293 (2004).
25. F. Gottrup, "Oxygen in wound healing and infection," *World J. Surg.* **28**(3), 312–315 (2004).
26. H. W. Hopf, T. K. Hunt, H. Scheuenstuhl, J. M. West, L. M. Humphrey, and M. D. Rollins, "Methods of measuring oxygen in wounds," *Methods Mol. Med.* **78**, 389–416 (2003).
27. H. W. Hopf, T. K. Hunt, H. Scheuenstuhl, J. M. West, L. M. Humphrey, and M. D. Rollins, "Measuring oxygen in wounds," *Methods Enzymol.* **381**, 539–564 (2004).
28. S. Bornmyr, A. Martensson, H. Svensson, K. G. Nilsson, and P. Wollmer, "A new device combining laser Doppler perfusion imaging and digital photography," *Clin. Physiol.* **16**(5), 535–541 (1996).
29. S. Langer, F. Born, R. Hatz, P. Biberthaler, and K. Messmer, "Orthogonal polarization spectral imaging versus intravital fluorescent microscopy for microvascular studies in wounds," *Ann. Plast. Surg.* **48**(6), 646–653 (2002).
30. M. C. Pierce, J. Strasswimmer, B. H. Park, B. Cense, and J. F. de Boer, "Birefringence measurements in human skin using polarization-sensitive optical coherence tomography," *J. Biomed. Opt.* **9**(2), 287–291 (2004).
31. Y. A. Pan and J. R. Sanes, "Non-invasive visualization of epidermal responses to injury using a fluorescent transgenic reporter," *J. Invest. Dermatol.* **123**(5), 888–891 (2004).
32. T. H. Helbich, T. P. Roberts, M. D. Rollins, D. M. Shames, K. Turetschek, H. W. Hopf, M. Muhler, T. K. Hunt, and R. C. Brasch, "Noninvasive assessment of wound-healing angiogenesis with contrast-enhanced MRI," *Acad. Radiol.* **9**(Suppl. 1), S145–147 (2002).
33. R. F. Mattrey and D. A. Aguirre, "Advances in contrast media research," *Acad. Radiol.* **10**(12), 1450–1460 (2003).
34. D. Huang, et al., "Optical coherence tomography," *Science* **254**(5035), 1178–1181 (1991).
35. X. D. Li and J. G. Fujimoto, "Optical Coherence Tomography," in *Encyclopedia of Biomaterials and Biomedical Engineering*, G. L. Bowlin and G. E. Wnek, Ed., pp. 1120–1132, Marcel Dekker, New York (2004).
36. A. T. Yeh, B. S. Kao, W. G. Jung, Z. P. Chen, J. S. Nelson, and B. J. Tromberg, "Imaging wound healing using optical coherence tomography and multiphoton microscopy in an in vitro skin-equivalent tissue model," *J. Biomed. Opt.* **9**(2), 248–253 (2004).
37. S. M. Srinivas, J. F. de Boer, H. Park, K. Keikhanzadeh, H. E. L. Huang, J. Zhang, W. Q. Jung, Z. P. Chen, and J. S. Nelson, "Determination of burn depth by polarization-sensitive optical coherence tomography," *J. Biomed. Opt.* **9**(1), 207–212 (2004).
38. B. H. Park, C. Saxer, S. M. Srinivas, J. S. Nelson, and J. F. de Boer, "*In vivo* burn depth determination by high-speed fiber-based polarization sensitive optical coherence tomography," *J. Biomed. Opt.* **6**(4), 474–479 (2001).
39. J. F. de Boer, S. M. Srinivas, A. Malekafzali, Z. P. Chen, and J. S. Nelson, "Imaging thermally damaged tissue by polarization sensitive optical coherence tomography," *Opt. Express* **3**(6), 212–218 (1998).
40. M. C. Pierce, R. L. Sheridan, B. H. Park, B. Cense, and J. F. de Boer, "Collagen denaturation can be quantified in burned human skin using polarization-sensitive optical coherence tomography," *Burns* **30**(6), 511–517 (2004).
41. Y. Hori, Y. Yasuno, S. Sakai, M. Matsumoto, T. Sugawara, V. D. Madjarova, M. Yamanari, S. Makita, T. Araki, M. Itoh, and T. Yatagai, "Automatic characterization and segmentation of human skin using three-dimensional optical coherence tomography," *Opt. Express* **14**(5), 1862–1877 (2006).
42. J. Weissman, T. Hancewicz, and P. Kaplan, "Optical coherence tomography of skin for measurement of epidermal thickness by shapelet-based image analysis," *Opt. Express* **12**(23), 5760–5769 (2004).
43. J. Pan and W. J. Tompkins, "A real-time QRS detection algorithm," *IEEE Trans. Biomed. Eng.* **32**, 230–236 (1985).
44. J. Canny, "A computational approach to edge-detection," *IEEE Trans. Pattern Anal. Mach. Intell.* **8**(6), 679–698 (1986).
45. Y. Masutani, H. MacMahon, and K. Doi, "Computerized detection of pulmonary embolism in spiral CT angiography based on volumetric image analysis," *IEEE Trans. Med. Imaging* **21**(12), 1517–1523 (2002).
46. A. P. Condurache and T. Aach, "Vessel segmentation in angiograms using hysteresis thresholding," in *Proc. MVA*, pp. 269–272 (2005).
47. R. Poli and G. Valli, "An algorithm for real-time vessel enhancement and detection," *Comput. Methods Programs Biomed.* **52**(1), 1–22 (1997).
48. A. Knuttel and M. Boehlau-Godau, "Spatially confined and temporally resolved refractive index and scattering evaluation in human skin performed with optical coherence tomography," *J. Biomed. Opt.* **5**(1), 83–92 (2000).
49. G. Odland and R. Ross, "Human wound repair. I. Epidermal regeneration," *J. Cell Biol.* **39**(1), 135–151 (1968).
50. S. S. Ramasastry, "Acute wounds," *Clin. Plast. Surg.* **32**(2), 195–208 (2005).
51. V. J. Mandracchia, K. J. John, and S. M. Sanders, "Wound healing," *Clin. Podiatr Med. Surg.* **18**(1), 1–33 (2001).
52. M. L. Usui, R. A. Underwood, J. N. Mansbridge, L. A. Muffley, W. G. Carter, and J. E. Olerud, "Morphological evidence for the role of suprabasal keratinocytes in wound reepithelialization," *Wound Repair Regen* **13**(5), 468–479 (2005).
53. R. Drezek, A. Dunn, and R. Richards-Kortum, "Light scattering from cells: Finite-difference time-domain simulations and goniometric measurements," *Appl. Opt.* **38**(16), 3651–3661 (1999).
54. American National Standard for the Safe Use of Lasers, ANSI Z136.1-1993, The Laser Institute of America, Orlando, Fla. (1993).
55. J. F. de Boer, B. Cense, B. H. Park, M. C. Pierce, G. J. Tearney, and B. E. Bouma, "Improved signal-to-noise ratio in spectral-domain compared with time-domain optical coherence tomography," *Opt. Lett.* **28**(21), 2067–2069 (2003).
56. A. F. Fercher, C. K. Hitzenberger, G. Kamp, and S. Y. Elzaiat, "Measurement of intraocular distances by backscattering spectral interferometry," *Opt. Commun.* **117**(1–2), 43–48 (1995).
57. G. Hausler and M. W. Lindner, "'Coherence radar' and 'spectral radar'—New tools for dermatological diagnosis," *J. Biomed. Opt.* **3**(1), 21–31 (1998).

58. R. Leitgeb, C. K. Hitzenberger, and A. F. Fercher, "Performance of Fourier domain vs. time domain optical coherence tomography," *Opt. Express* **11**(8), 889–894 (2003).
59. R. A. Leitgeb, W. Drexler, A. Unterhuber, B. Hermann, T. Bajraszewski, T. Le, A. Stingl, and A. F. Fercher, "Ultrahigh resolution Fourier domain optical coherence tomography," *Opt. Express* **12**(10), 2156–2165 (2004).
60. J. A. Izatt, M. D. Kulkami, S. Yazdanfar, J. K. Barton, and A. J. Welch, "*In vivo* bidirectional color Doppler flow imaging of picoliter blood volumes using optical coherence tomograghy," *Opt. Lett.* **22**(18), 1439–1441 (1997).
61. Z. P. Chen, T. E. Milner, D. Dave, and J. S. Nelson, "Optical Doppler tomographic imaging of fluid flow velocity in highly scattering media," *Opt. Lett.* **22**(1), 64–66 (1997).